Supporting Information for “”Femtosecond laser induced resonant tunneling in an individual quantum dot attached to a nanotip”

Maxime Duchet,[1] Sorin Perisanu,[1] Stephen T. Purcell,[1] Eric Constant,[1] Vincent Loriot,[1] Hirofumi Yanagisawa,[2] Matthias F. Kling,[2,*] Franck Lepine,[1] and Anthony Ayari[1]

[1] *Univ Lyon, Univ Claude Bernard Lyon 1, CNRS, Institut Lumière Matière, F-69622, VILLEURBANNE, France.*

[2] *Department of Physics, Ludwig-Maximilians-Universität Munich, Am Coulombwall 1, 85748 Garching, Germany.*

*Also at Max Planck Institute of Quantum Optics. Hans-Kopfermann-Straße 1, 85748 Garching, Germany

Contents

I. ADDITIONAL DESCRIPTION OF THE EXPERIMENT AND DATA ANALYSIS

The experiments (see Fig. S1) were performed in a chamber allowing to perform standard field emission measurements, as described in [S1] p.197 or in [S2–S4] for femtosecond experiments on nanotips with a focused femtosecond laser, as well as *in situ* nanostructuration and electron energy analysis.

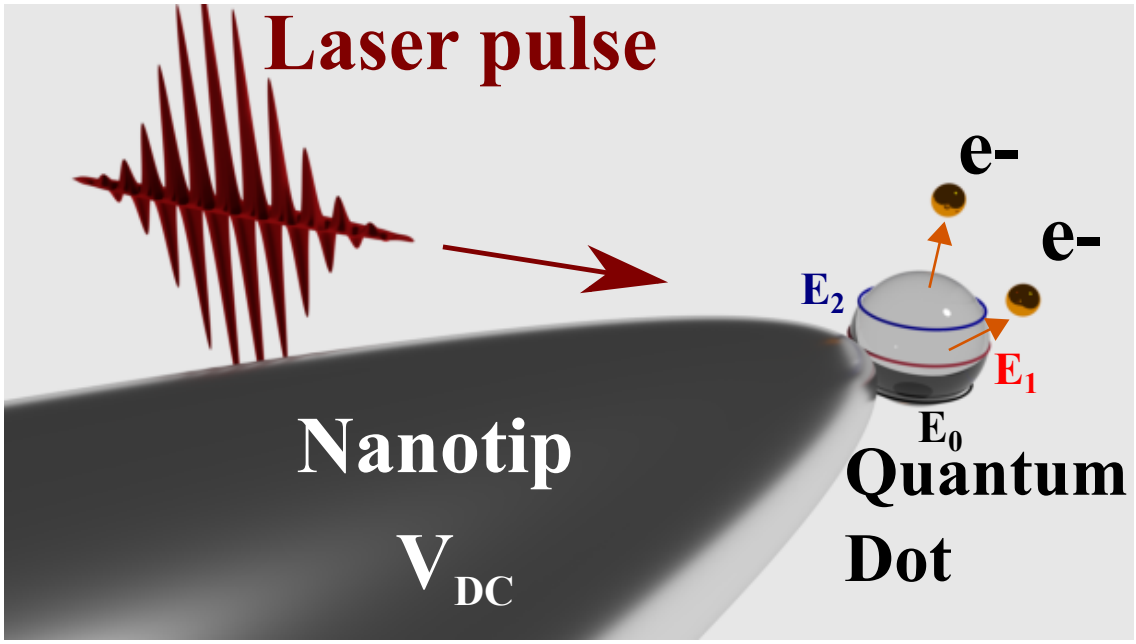

FIG. S1: Excitation of a nano-object on a tungsten tip by a femtosecond laser.

A. Ex situ tip fabrication:

The nanotip was fabricated from a tungsten (W) <111> single crystal wire with an initial diameter of 150 μm. The wire was cut to a length of less than 2 cm. Then it was electrochemically etched in a NaOH solution to form a sharp tip with a radius below 50 nm.

B. Optical set-up:

The optical experiments were performed with a Ti:sapphire laser oscillator with f = 80 MHz repetition rate, a spectrum centered around 800 nm (photon energy $h\nu$ =

1.55 eV), a pulse duration of 14 fs and 300 mW maximum output power. The laser is focused, with an off-axis parabolic mirror with focal length of 5 cm, to a waist w of 5 μm. The light polarization is chosen parallel to the tip shank.

C. Spectral phase of the laser pulse:

The measurement of the spectral phase of our laser was performed by the FROG (Frequency-resolved optical gating) technique, see Fig. S2.

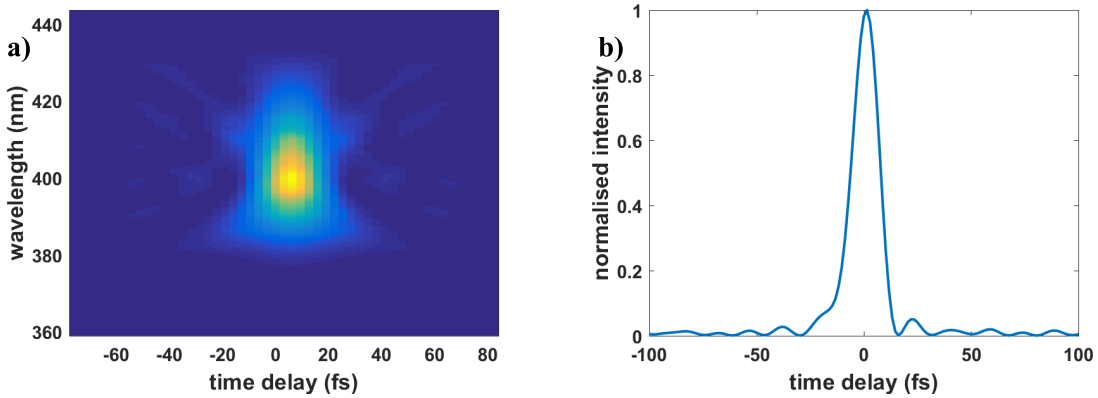

FIG. S2: a) Frequency-resolved optical gating (FROG) of the Ti:sapphire laser oscillator after optimization, b) Temporal profile of the laser pulse, with full width at half maximum (FWHM) of 14.2 fs.

D. Field emission set–up:

The ultra-high vacuum (UHV) field emission chamber used in this study operated at a base pressure of 5×10^{-10} Torr. The tungsten tip is mounted on a X, Y, Z stick-slip piezoelectric translation stage in order to bring the tip into the region of highest laser intensity. The translation stage and the chamber were grounded as well as the optical mirror mount. The field emission set-up has the W tip as the emission cathode, an extraction anode, three hemispherical grids, a two-stage microchannel plate (MCP) and a phosphor screen. The cathode is set to a negative voltage V_c (typically – 90 V) and the extraction anode is set to a positive voltage V_e (100's of Volts). The DC voltage specified in the experiments is the voltage difference between the anode and the cathode. The front face of the MCP

is grounded. The emitted electrons from the cathode are collected by the two-stage MCP biased at a DC voltage between 1500 and 2000 V in order to amplify the current. The electrons at the output of the MCPs are then accelerated towards a phosphor screen to emit photons representing the spatial distribution of the emitted electrons. This emission pattern is then visualized with a camera.

E. Retarding field energy analyzer:

The retarding field analyzer is composed of three grids operated at different voltages. A DC bias and small AC bias is applied on the grid in the middle. The DC bias is swept around the voltage of the emission tip and will select the electrons by repelling those with a kinetic energy below the sum of the grid voltage and the grid work function. V_g is the sum of the DC and AC voltages. The voltage difference between the grids is fixed at V_b =1.5 V in order to improve the energy resolution. The current on the phosphor screen is collected by a variable gain, home-made, electrically floating, trans-impedance amplifier. The DC output of the amplifier is recorded by a digital voltmeter and the AC signal is measured with a lock-in amplifier in order to get the voltage derivative of the DC current. This AC current gives the electron energy spectrum and has less noise than a numerical derivative of the DC signal.

F. Analysis of the retarding field energy analyzer current:

As the lock-in records also the AC current noise at the oscillation frequency it measures also the electron shot noise and an additional excess noise. This noise is similar in shape and instrumental origin to the background noise observed in X-ray photoelectron spectroscopy (XPS). It is proportional to the square root of the lock-in time constant and can be made unobservable by reducing the lock-in bandwidth which requires to sweep the voltage more slowly. In order to reduce the acquisition time of the spectrum we removed numerically this background noise by applying a skewness factor correction to the data as in XPS experiments.

In mathematical terms, the current on the phosphor screen can be written as $I(t, V_g)$ since it depends on the voltage V_g on the grid that filters the electron kinetic energy as explained in the paragraph above and as shown in Fig. S3 for sample QD1 where V_g has

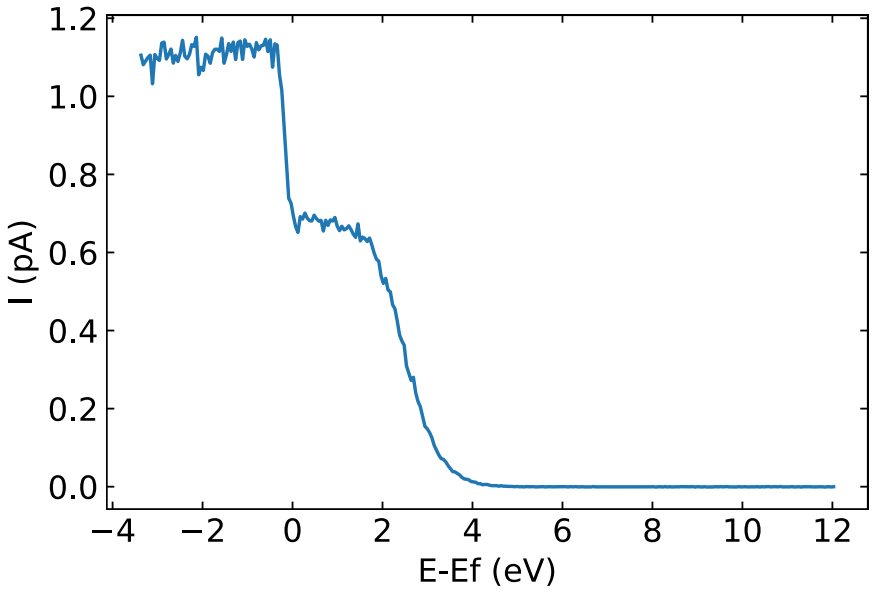

FIG. S3: Amplified DC current measured on the phosphor screen for a laser intensity of 10 mW and an applied voltage V_{DC} = 290 V on the electron emitter QD1.

been expressed in terms of energy. The work function of the grid is unambiguously measured with the spectrum from the clean W tip and has been used to fix the zero. In figure S3, at low energy (or grid voltage V_g) all the emitted electrons are collected on the MCP. A first drop of current is observed for an energy close to the Fermi energy due to the fact that the energy analyzer filters the electrons from E_0. A second drop is also observed when the repelling potential from the grid is raised above the kinetic energy of the electrons emitted by the energy level E_2. The numerical derivative of this curve can be calculated to give the electron energy spectrum $J(E)$. The expression of the current is $I(t, V_g) = \bar{I}(V_g) + \tilde{I}(t)$ with:

$$\bar{I}(V_g) = \int_0^{eV_{DC}+E_F-qV_g-\phi_g} J(E)dE \tag{S1}$$

where V_{DC} is the applied DC voltage on the quantum dot, ϕ_g is the grid work function and $\tilde{I}(t)$ the current noise from the emitter.

For better signal to noise ratios, we use a lock-in setup. The voltage grid is composed of a DC bias and a small AC bias at the lock-in frequency ω, $V_g = V_g^{DC} + V_g^{AC} \cos \omega t$. So the measured current is:

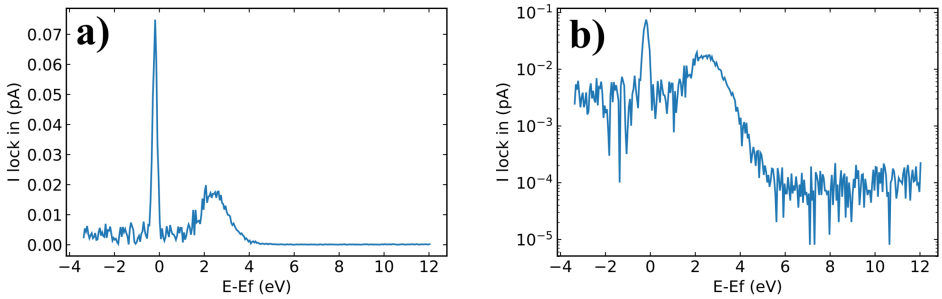

FIG. S4: a) Experimental electron energy spectrum of a quantum dot before signal correction measured simultaneously with the curve shown on Fig. S3. b) Same data as in a) in log scale.

$$\bar{I}(V_g) \approx \bar{I}(V_g^{DC}) + \frac{\partial \bar{I}}{\partial V_g} V_g^{AC} \cos \omega t + \tilde{I}(t) \tag{S2}$$

By Fourier transform, we obtain the current measured by the lock-in:

$$I^{LI}(\omega) = \sqrt{\left(\frac{\partial \bar{I}}{\partial V_g} V_g^{AC}\right)^2 + S_{\tilde{I}}(\omega)\Delta\omega} \tag{S3}$$

where $S_{\tilde{I}}$ is the noise power spectrum density and $\Delta\omega$ is the lock-in bandwidth. The term $\partial\bar{I}/\partial V_g$ is proportional to J as can be deduced from Eq. S1. Fig. S4 shows the raw data of a typical spectrum measured on QD1 by the lock-in. On the low energy side, the signal is noisier and in log scale a plateau is clearly visible on the low energy side as well as a lower plateau on the high energy side. The plateau on the high energy side is given by the noise back ground of our electronics. On the other hand, the plateau on the low energy side comes from the emitter noise (the $S_{\tilde{I}}$ term). To confirm this point, we performed the following test: i) we changed V_g^{AC} and observed that the plateau remained unchanged while the peak increase linearly; ii) we changed the bandwidth of the lock in and observed that the peak remained unchanged while the plateau increased with the square root of the lock in bandwidth; iii) we changed the current from the quantum dot and observed that the plateau increased with the square root of the emitted current. This last point indicates that the main source of noise is the shot noise of the emitted electron $S_{\tilde{I}} = 2eI^{DC}$. This explains why the plateau disappears at high energy as in that case the emitted electrons are filtered and so thus the noise disappears. Therefore, the noise decreases gradually as the energy is swept through the emission peaks.

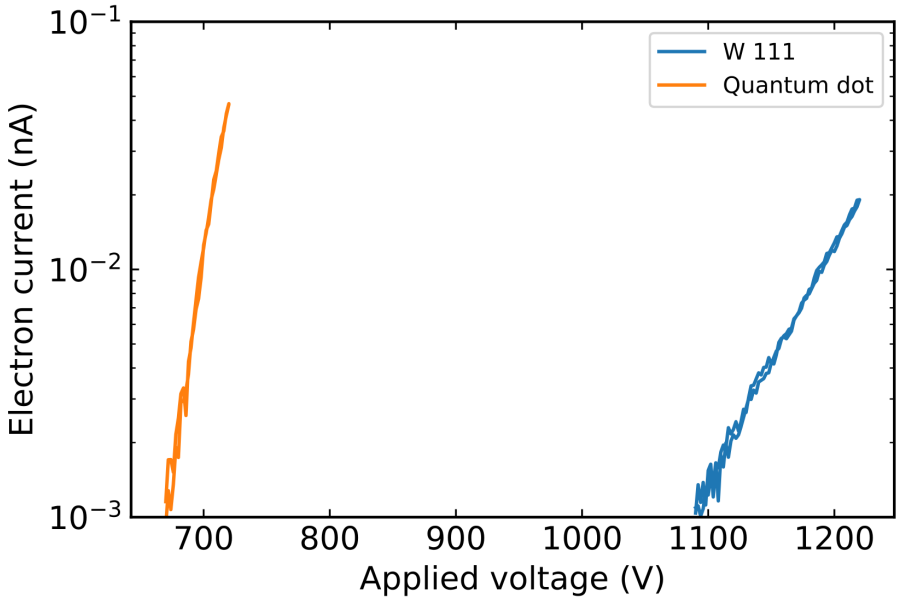

FIG. S5: Measured voltage-current curve for a clean W111 tip and the same tip with a quantum dot.

G. In situ sample preparation:

The cathode can be in situ cleaned by standard Joule heating of a resistive loop attached by spot welding on the W wire. Our quantum dot synthesis method is based on field-driven diffusion which tends to build sharper forms (such as with Taylor cones) on the tip apex to minimize electrostatic energy[S5]. It has the advantages of a high yield of fabrication, on-axis positioning, reproducibility without breaking vacuum and tunability of the nano-object size with Ångström accuracy. The obtained nanostructure has been characterized through its emission pattern and field emission properties. The metallic tip is first heated to high temperature to remove surface adsorbates. The cleanliness of the tip is confirmed by observing the field emission patterns of expected symmetry on a MCP with a negative voltage, $-V_0$, on the tip giving an emission current of $\sim$1 pA. After cleaning the tip temperature is gently increased from room temperature to a temperature T_0 (about 500 K) where the pattern starts to fluctuate. Then a positive voltage is applied on the tip at a value roughly $1.5V_0$ and a temperature 10% above T_0 for 30 s. This first step leads to the formation of a "buildup" tip[S5] with lower electron emission voltage and a more pronounced emission at the center. The second step consists in controlling the negative

voltage on the tip so that the emission current is about 100 nA for 10 minutes. The required voltage decreases gradually because of the formation of the nano-object with higher field enhancement. At the end of the process, the emission voltage for the original current has decreased and the pattern has a single bright spot. In our experiments, the required voltage to obtain an emission current of a few pA is typically divided by a factor of two compared to the initial metal tip before growth. Fig. S5 illustrates that on the same tip before the formation of the quantum dot, the voltage necessary to emit the same current is twice as big as after the formation of the quantum dot.

Despite many studies over several decades, we consider that the chemical composition of such nanostructures is still an open question. But more importantly the peculiar voltage dependence of the electron energy spectrum is observed for nanotips made of different materials and in different experimental configurations. So this means that the phenomenon is rather universal and independent of the exact chemical composition. In ref. [S6] and [S7] W or Pt nanotips were fabricated. It was proposed that the nanostructure consists of single-atom sharpness nanoprotrusions, 2−5 nm height, on top of hemispherical base tips. In ref.[S8] tungsten carbide-coated W <111>, HfC <100> and ZrC <100> emitters were studied and showed similar behavior. Again the emission was supposed to come from a single atom due to the field ion microscopy patterns. The authors noticed that carburization of the tip surface was essential to obtain their built-up tips. So they considered that the spacer between the bulk tip and the single atom was a single carbon atom or an aggregate of carbon atoms. In ref. [S9] Mo <100> were fabricated and Auger electron spectroscopy seemed to indicate that Ca segregates from the bulk and forms the nanoprotusion. Finally, in ref. [S10] the authors noticed that even at room temperature this kind of nanotip could be fabricated without any particular procedure. They mentioned that they planned to use atom probe methods in order to identify the species of the nanoprotusion but we are not aware of any published results concerning such a study. From this work and knowing the typical composition of residual gas in a UHV chamber as measured for instance in [S11] we consider that the nanostructure is probably formed of tungsten atoms on top of a contamination layer or carbon mono-oxide due to its large sticking coefficient and because it is the most important residual gas molecule in UHV after hydrogen.

H. Data on a clean W field emitter:

We give here some data from a clean W field emitter. Figure S6 presents the electron energy spectra and the emission patterns before the nano-object growth. For a W nanotip, the energy peak is centered closed to E_F and its position is mostly unchanged when the DC voltage is increased while the width of the peak increases slightly on the low energy side (i.e. below E_F). The temperature for tip cleaning was limited in order to maintain a low apex radius and thus a high field enhancement. Thus the field emission pattern as presented in the inset of Figure S6 was not totally rounded.

Figure S7 shows the distribution of the emitted electrons from the W tip without the quantum dot just before its growth and just after its removal. The spectrum is plotted as a function as the absolute value of the applied grid voltage and not as a function as the electron energy in order to show how the calibration of the Fermi energy is done and what is its uncertainty. The voltage applied on the tip is -500 V and the voltage on the extraction anode is + 500V, the voltage grid has been swept between -494 V and - 497 V. The peak intensity has changed by a factor of 2 which is typical in field emission, as the tip never

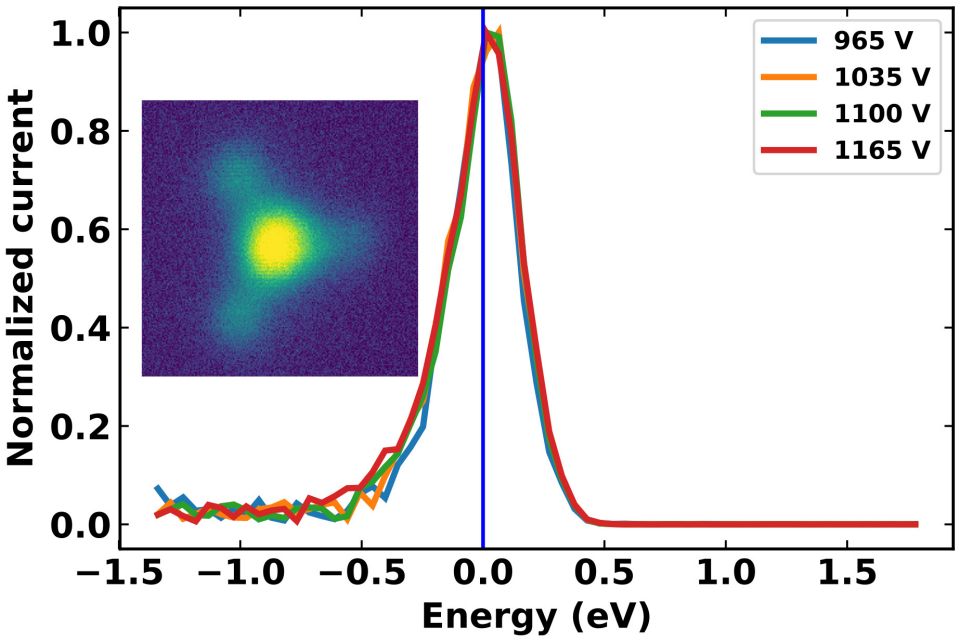

FIG. S6: Experimental energy spectrum of the emitted electrons from a clean W<111> tip for different applied DC voltages. Inset: field emission pattern of the W tip.

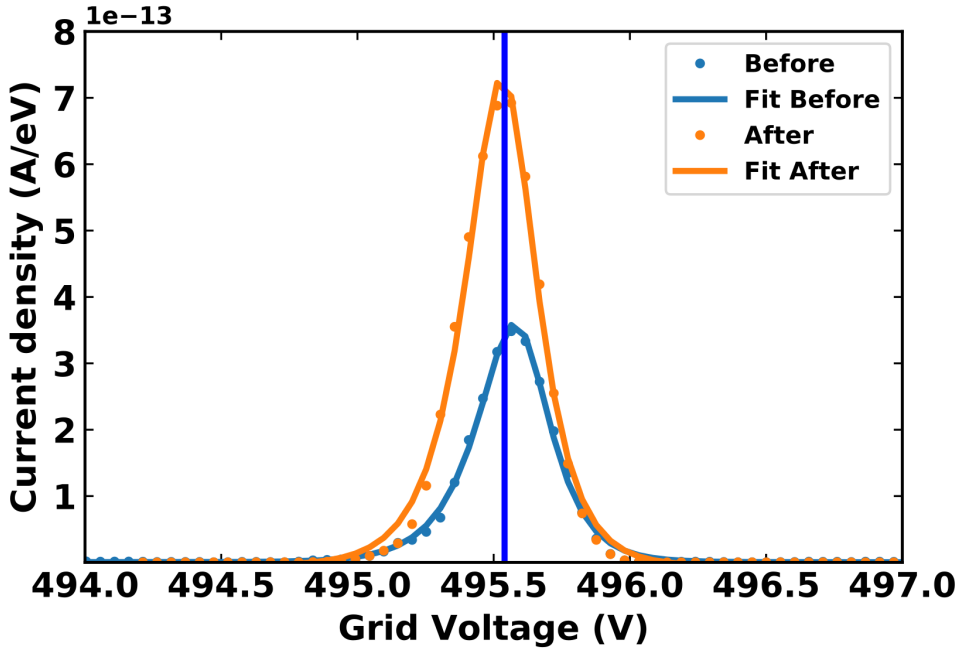

FIG. S7: Experimental energy spectrum of the emitted electrons from a clean W<111> tip at an applied DC voltage $V_{DC} = 1000$ V before the growth of the nano-object and after its removal. The dots are the data points and the solid lines are a fit of the corresponding data. The vertical line represents the position of the Fermi energy after removal of the quantum dot.

totally recovers its exact shape between successive cleaning procedures. The two peaks have been fitted by the classical total energy distribution formula [S12, S13] to extract the Fermi energy. We obtained 495.59 V before the QD fabrication and 495.54 V after. We consider the typical uncertainty in the determination of the Fermi energy is between +/-50 meV for our retarding field analyzer if the the tip emission is in the center of the screen. If we include other factors such as the instability of the quantum dot, the uncertainty in peak energy close to the Fermi energy is +/-100 meV. Finally, although the tip voltage is -500 V, the grid repels the electrons at a voltage around -495.5 V because of the work function of the grid : the electrons tunnel from the Fermi level of the tip but electrons are blocked by the top of the barrier of the grid which is given by the position of the Fermi energy of the grid plus the work function of the grid.

Figure S8 shows the evolution of the energy spectrum of the clean W<111> tip for different voltages and a laser intensity identical to the one of Figure 4a of the main text. It can be seen that the required voltage is much higher here. Below 600 V, no signal can

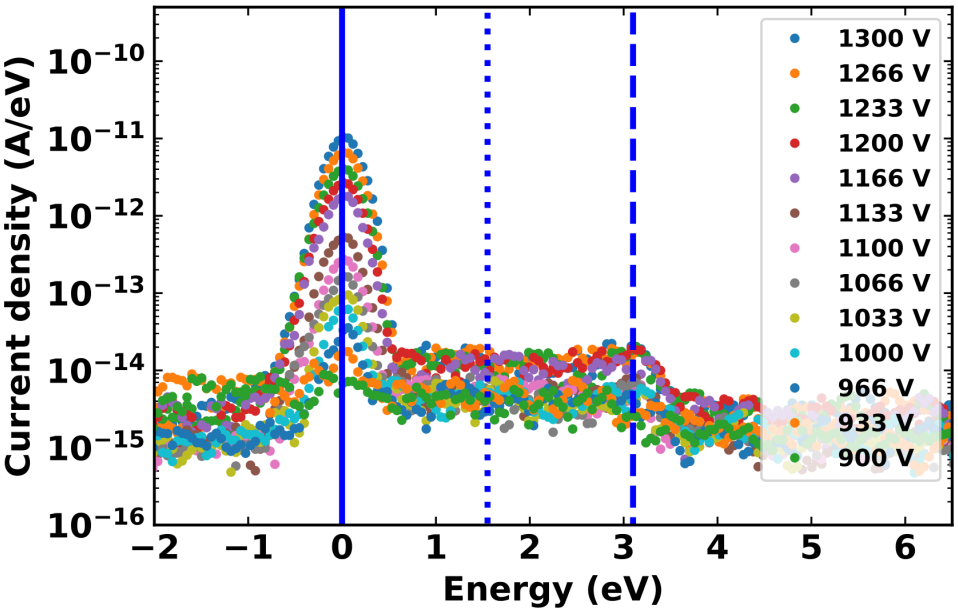

FIG. S8: Experimental energy spectrum of the emitted electrons from a clean W<111> tip for different applied DC voltages at a fixed laser power of 10 mW. The vertical line represents the position of E_F inside the W tip. The vertical dotted (respectively dashed) line indicates an emission energy $h\nu$ (respectively $2h\nu$) above E_F.

be measured. This indicates that in the case of the QD, the electrons are not emitted by the tip surrounding the nano-object. Although the surface of the tip and the laser spot size are much larger than the QD, all the extracted electrons travel through the nano-object. The interaction of the tip with the laser is also much less efficient as can be seen from the weakness of the $2h\nu$ peak. Probably, the most remarkable difference with the quantum dot is that the spectrum overall shape is unchanged by increasing the voltage, just the electron current increases.

Figure S9a shows the evolution of the energy spectrum of the clean W<111> tip for different laser intensities and a voltage higher than the one of Figure 3a of the main text. Again the signal from the tip is smaller than the signal from the quantum dot at similar voltages. The $2h\nu$ peak cannot be distinguished from the shot noise but the signal in the spectrum clearly decreases at this energy. In Figure S9b, we compare the tip emission with the quantum dot for an identical laser intensity and an identical total emitted current. It shows that in this condition also the shapes of the spectra are very different, indicating that

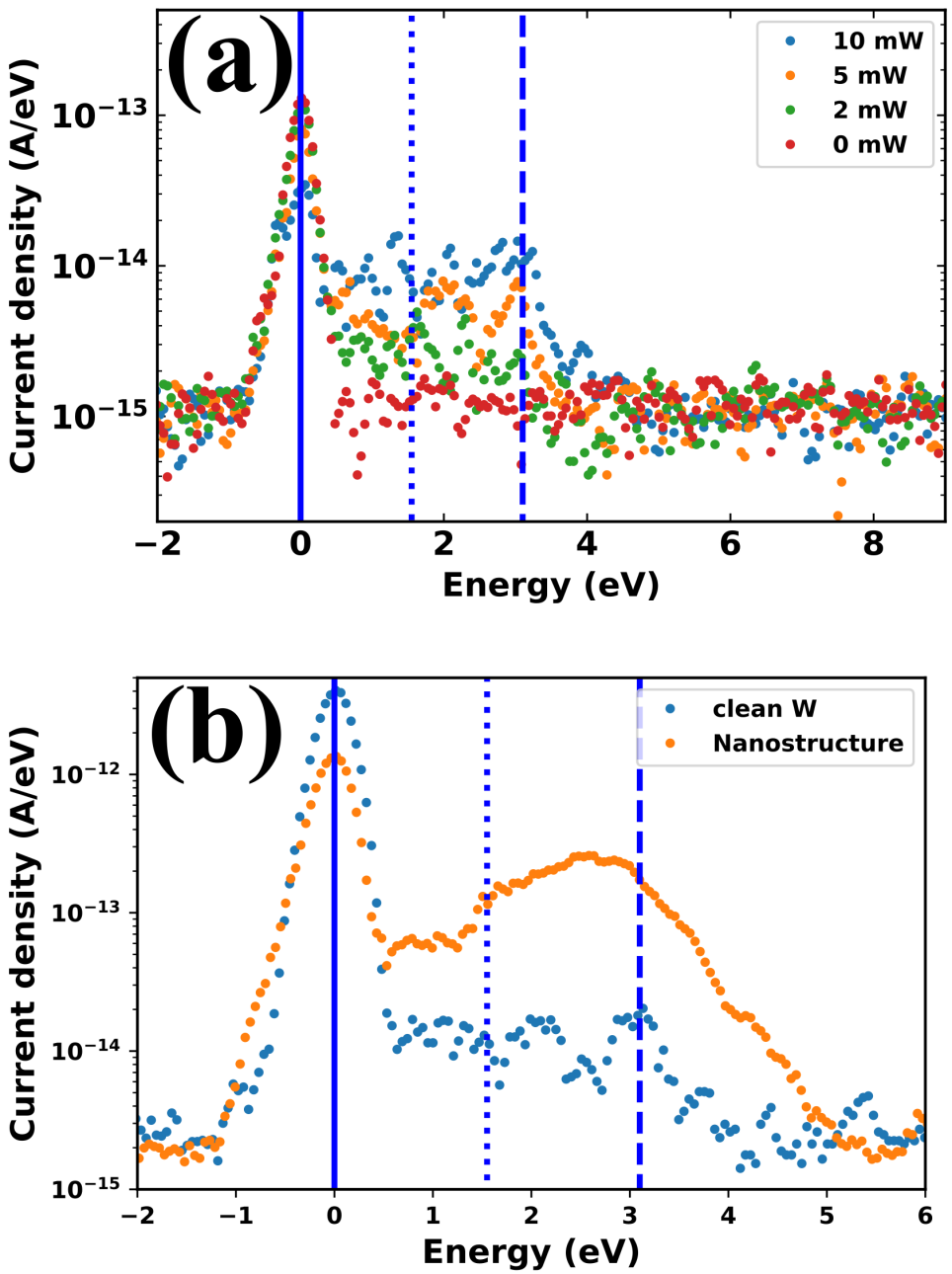

FIG. S9: a) Experimental energy spectrum of the emitted electrons from a clean W<111> tip for different laser intensities and a fixed DC voltage $V_{DC} = 1000$ V. b) Experimental energy spectrum of the emitted electrons from a clean W<111> tip for 10 mW and 1233V and from QD1 for 10 mW and 325 V. The vertical line represents the position of E_F inside the W tip. The vertical dotted (respectively dashed) line indicates an emission energy $h\nu$ (respectively $2h\nu$) above E_F.

it is not only a question of field enhancement.

II. DATA AND ANALYSIS ON OTHER QUANTUM DOTS

The experiments were performed on several quantum dots, of which in the publication we report results mainly on QD1. We present here data from other quantum dots.

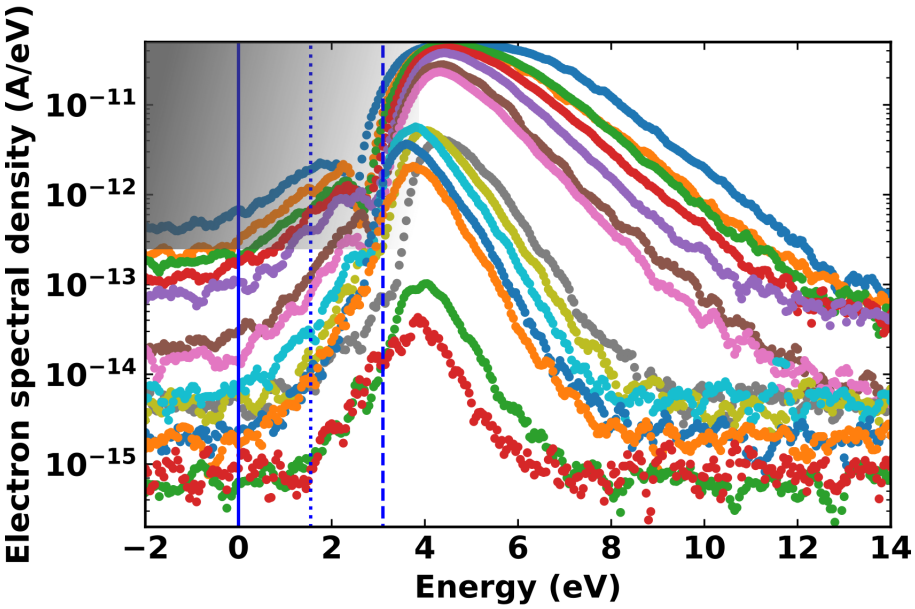

FIG. S10: Measured energy spectrum of the emitted electrons from QD7 for different femtosecond laser powers (from 20 mW to 150 mW with 10 mW steps) and a fixed applied voltage 100V. The vertical line represents the position of E_F inside the W tip. The vertical dotted line indicates an emission energy $h\nu$ above E_F. The vertical dashed line indicates an emission energy $2h\nu$ above E_F. The grey area in the left top corner indicates the zone where the MCP saturates.

A. QD7, high laser intensity:

QD7 has been studied for laser intensities up to three times higher than the laser intensities used for QD1. Similarly to what was observed for QD1, Fig.S10 shows an increase of the high energy peak when the laser power increases. The peak below the Fermi energy is barely visible at low laser power (30 mW) and is hidden by the shot noise of the high energy peak at higher laser powers.

Above 80 mW, only the part of the spectra with energies above approximately 6 eV are reliable because the MCP gain falls off when the output current is above several hundreds of

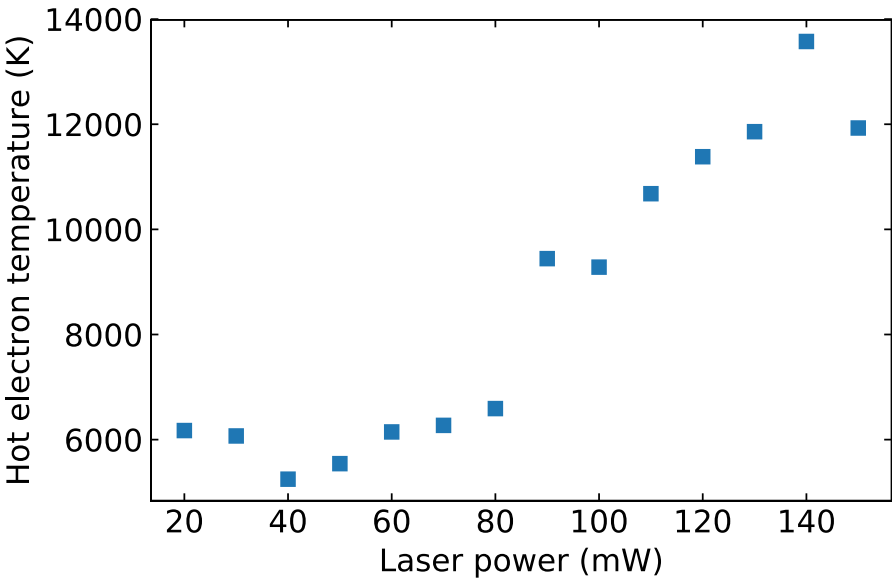

FIG. S11: Fitted effective electron temperature for QD7 at a voltage of $V_{DC} = 100$ V as a function of the laser power.

nA. For electron energies below this value the retarding field analyzer let too many electrons to pass through the grids, so the MCP saturates and the current measured on the phosphor screen is not well calibrated anymore.

From the spectral density of the emitted electron shown in Fig. S10, a fit of the exponential decay gives an effective temperature for high energy electrons. These temperatures are plotted in Fig. S11. For a power lower than 80 mW (*i.e.* 170 GW/cm^2) the effective temperature is rather constant in the 6000 K range. At higher power, QD7 shows an increase of this temperature that might come from some changes in the electron energy relaxation. A discussion about this effective temperature is given below in section III C for QD1.

Fig. S12 shows the evolution of the electron emission of the high energy peak. At low laser power this current was obtained by integration of the electron energy spectrum. However, for higher laser powers, we used the value of the current on the electrometer connected to the tungsten tip and not the one from the MCP because in such a regime the MCP is saturated on one side of the spectrum. As in this regime the high energy peak dominates, its integrated current is almost equal to the total current measured by the electrometer. The evolution of the current in log-log plot in Fig. S12 is linear and the fitted exponent of the

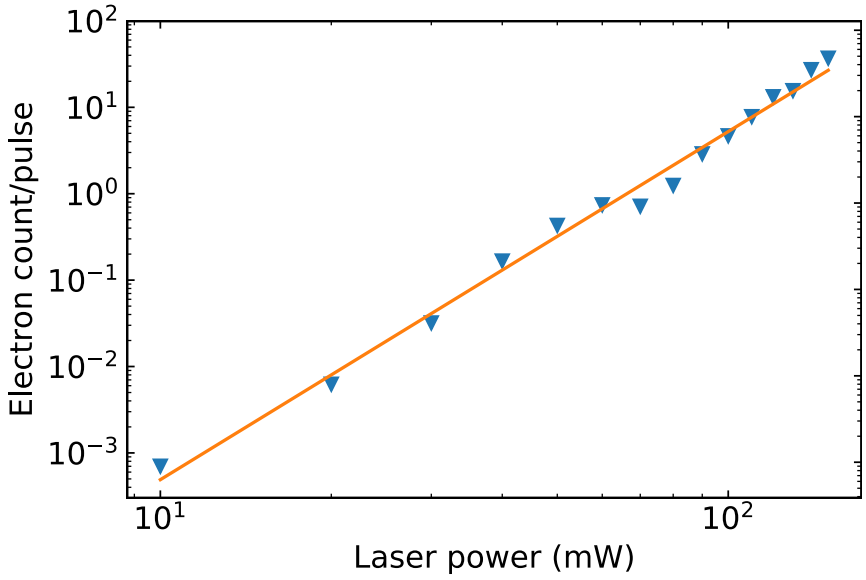

FIG. S12: Intensity of the high energy peak as a function of the laser power for QD7 at a voltage of V_{DC} = 100 V. The solid line is a fit of the experimental data.

power law is 4.02.

B. QD11, peak shift without laser:

QD11 was studied for different voltages without laser as a reference to show that our synthesis method produces quantum dots with a behavior identical to previous studies [S6, S10]. Fig. S13 shows that experimentally the distribution of the emitted electrons of a quantum dot shifts linearly with the applied electric field and this trend can be reproduced by numerical simulations as detailed in IV B.

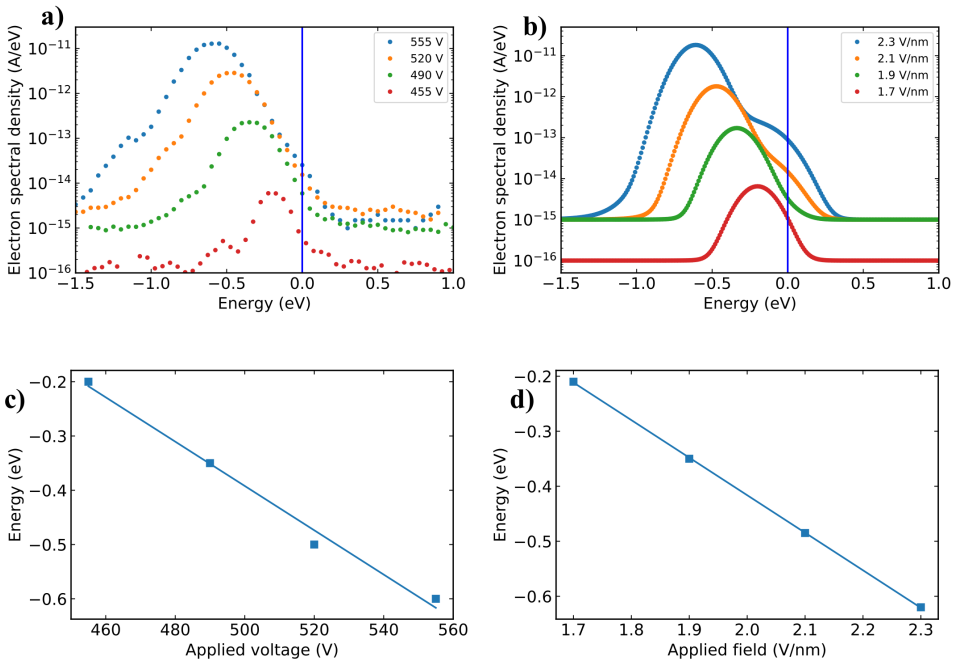

FIG. S13: a) Experimental energy spectrum of the emitted electrons from sample QD11 for different applied voltages. b) Simulated energy spectrum of the emitted electrons from sample QD11 for different electric fields. The vertical line represents the position of the Fermi energy inside the W tip. c) Experimental energy shift of the maximum of the energy peak as a function of the applied voltage. The line is a fit of the experimental data. d) Calculated energy shift of the maximum of the energy peak as a function of the electric field. The line is a fit of the simulated data.

C. QD12, voltage and laser dependence:

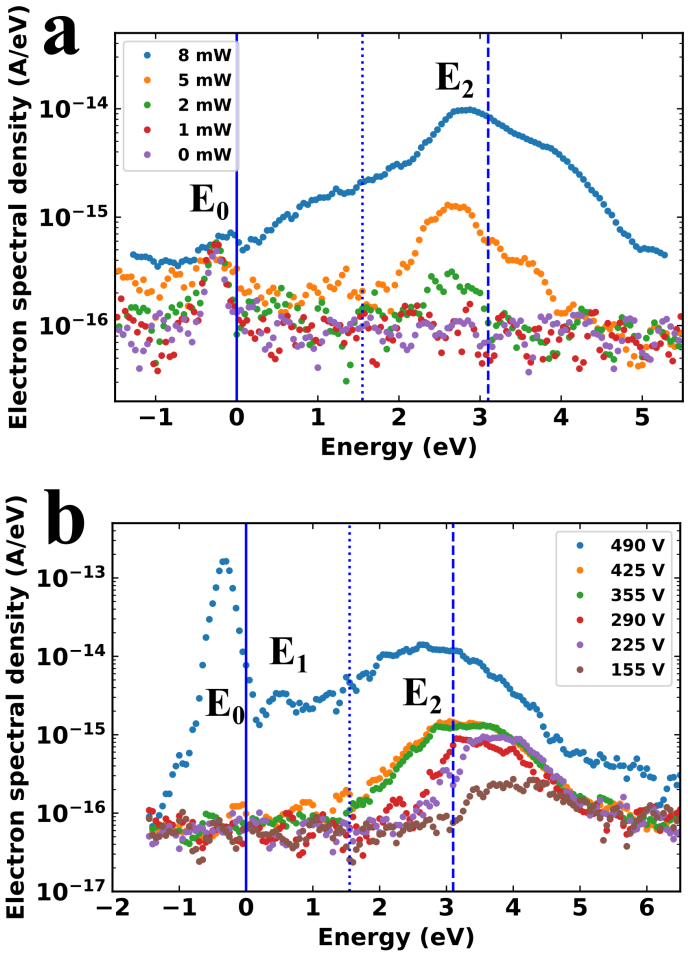

FIG. S14: a) Measured energy spectrum of the emitted electrons from QD12 for different laser powers and a fixed applied voltage of 355V. b) Measured energy spectrum of the emitted electrons from QD12 for different voltages and a fixed laser power of 10 mW. The vertical line represents the position of E_F inside the W tip. The vertical dotted line indicates an emission energy $h\nu$ above E_F. The vertical dashed line indicates an emission energy $2h\nu$ above E_F.

QD12 presents the same features as QD1. As in Fig. 3 of the main text, Fig. S14a shows, for QD12, a peak E_F below the Fermi energy and a high energy peak E_2 in between 2 photon energies. Similarly to QD1 (Fig.4 of the main text), in Fig. S14b, the high energy peak of QD12 shifts with the applied voltage, the low energy peak appears only for a high enough voltage i.e. when this level is below the Fermi energy. An intermediate peak E_1 starts to be visible for high enough voltage. The high energy peak is rather flat indicating

the presence of two close peaks that cannot be resolved due to the noise current.

D. QD17, peak shift with laser:

In Fig. S15, we present the voltage dependence of the spectral density of the emitted electron of QD17. its behavior is similar to the one observed in Fig.4 of the main text and in Fig. S14b

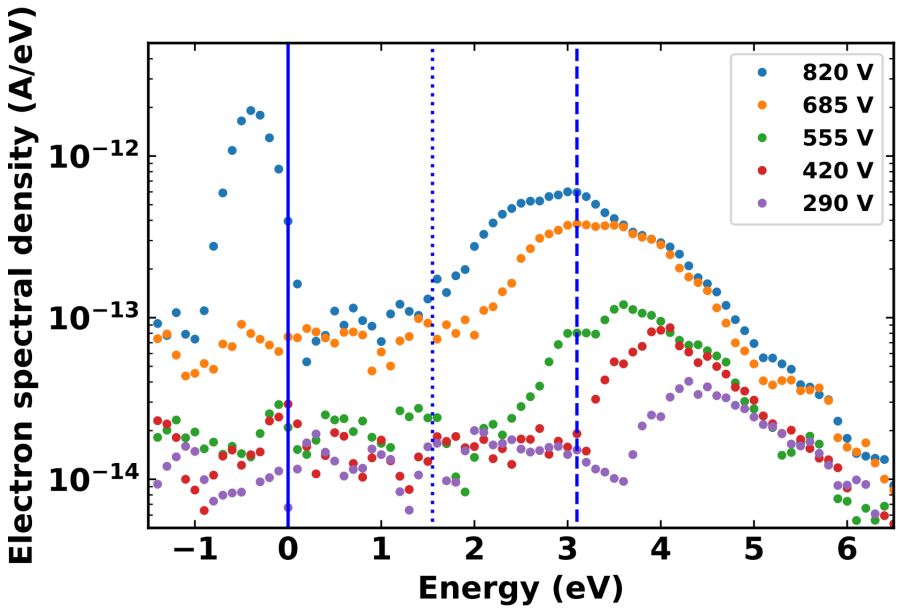

FIG. S15: Measured energy spectrum of the emitted electrons from QD17 for different voltages and a fixed laser power of 100 mW. The vertical line represents the position of E_F inside the W tip. The vertical dotted line indicates an emission energy $h\nu$ above E_F. The vertical dashed line indicates an emission energy $2h\nu$ above E_F.

III. ADDITIONAL DATA AND ANALYSIS FOR QD1

We present here some supplementary data and analysis on QD1

A. Shifting of the energy levels:

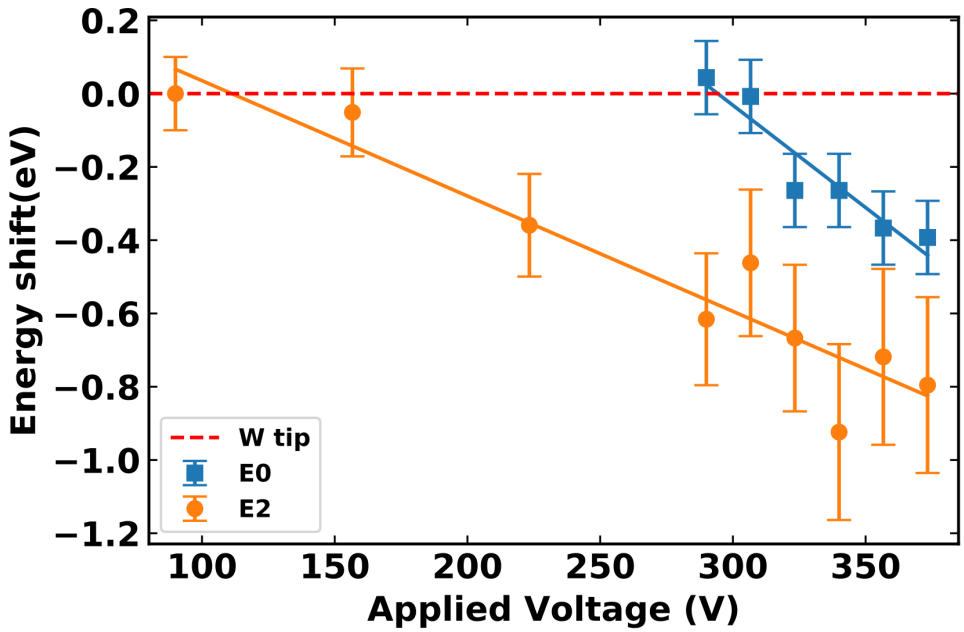

FIG. S16: Relative energy shift of the peaks maximum E_0 (square) and E_2 (circle) as the function of the applied voltage at a fixed laser power of 10 mW (21 GW/cm^2). The solid lines are a fit of the experimental data. The relative shift has been fixed at zero at the lowest measured voltage in order to highlight the difference in slope between the two peaks.

In the simple approach used in past works [S6, S14, S15] to interpret the results in field emission of quantum dots, the slope is the same for any energy level and is just determined by the electric field and the distance d of the quantum dot from the tip as explained in the main text. So in first approximation the shift in energy should be given by $\Delta E = eFd$. However this approach neglects the size a of the quantum dot and the fact that the electric potential might change significantly from one side to the other side of the quantum dot if a is comparable or larger than d. In such a case the spatial extent of the wave function is different for each energy levels and so the influence of the electric field will depend on the eigenstates. Fig. S16 shows that this slope is different for different energy levels on the same

quantum dot. This representation emphasizes better the difference in slope that in the Fig. 4c of the main text which based on the same data.

B. Disappearance of the peak E_0 for low voltages:

In Fig. 4 of the main text, the peak E_0 is not visible for $V < 290$. This effect is due to the linear peak shift with voltage as shown in Fig. S13 and S16. Experimentally Fig. 4c of the main text clearly shows that E_0 crosses E_F at 290 V. As illustrated in Fig. S17a (respectively b), for $V > 290$ V (respectively $V < 290$ V), E_0 is below (respectively above) the Fermi energy. It means that in the absence of laser, no electron from the tip would have enough energy to travel through this energy level for $V < 290$ V. In the presence of a laser, the electronic distribution is not described by a Fermi Dirac distribution but the density of electrons drops by several orders of magnitude (in Fig. S17, this distribution is represented in log scale in order to enhance the visibility). So the intensity of the peak E_0 will also drop by several orders of magnitude if V decreases below 290 V. Its intensity will even be below the intensity of E_1, because the electron distributions of E_0 and E_1 in this configuration are rather close whereas the barrier transmission for E_0 is much smaller that the transmission for E_1. As E_1 is barely visible, E_0 is undetectable for $V < 290$ V

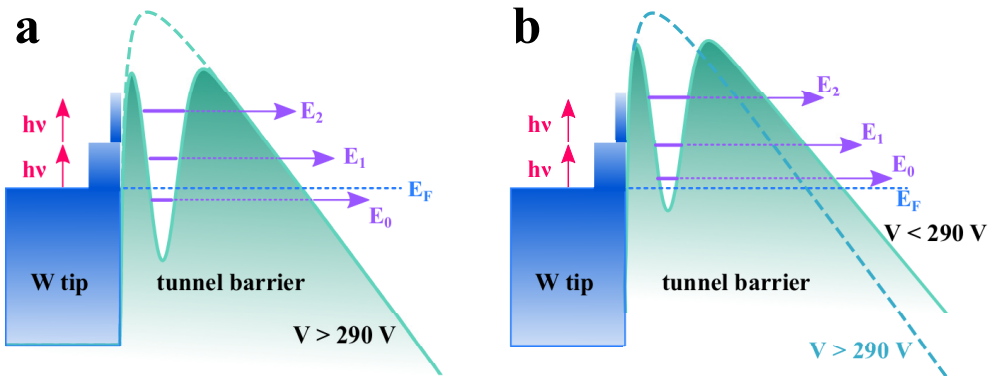

FIG. S17: a) Energy band diagram of the tunneling barrier for field emission with a quantum dot for $V > 290$ V. The dotted line represents the tunneling barrier in the absence of the quantum dot. E_0 is below the Fermi energy E_F b) Energy band diagram for $V < 290$ V. The dotted line represents the tunneling barrier in the absence of the quantum dot for the same voltage V as in a) for comparison.

C. Effective temperature of the hot electrons emitted by the quantum dot with laser on:

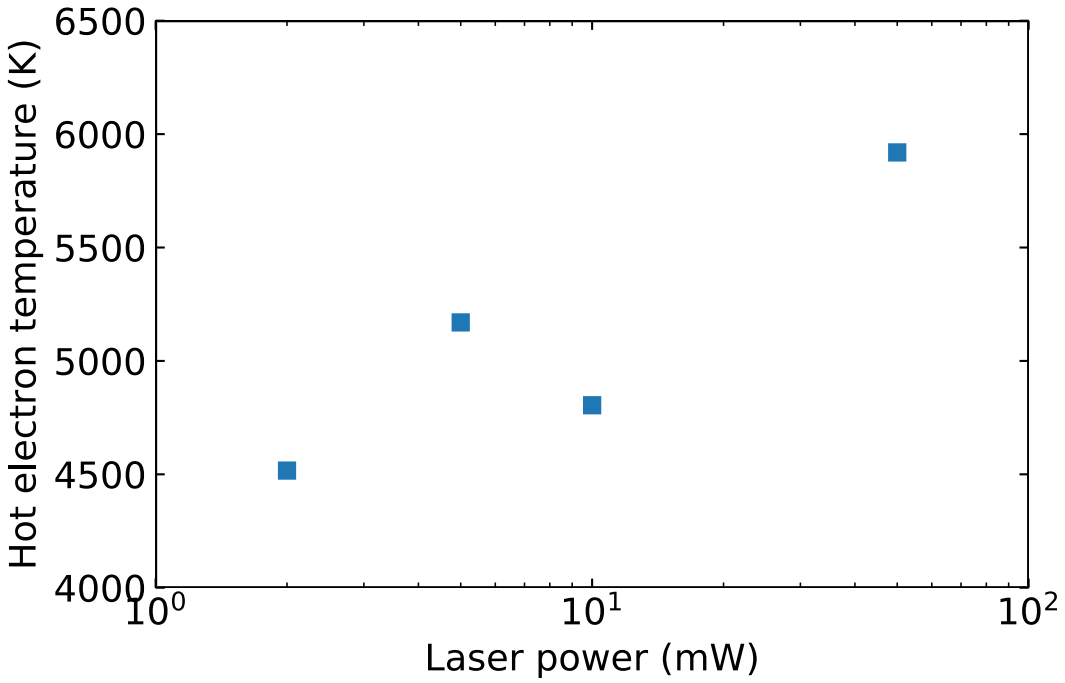

FIG. S18: Fitted effective electron temperature for QD1 at a voltage of $V_{DC} = 290$ V as a function of the laser intensity.

The high energy part of the spectra Fig. 3a of the main text has an exponential decay with electron energy, as shown by the linear dependence of the current in the semi-log representation, $I(E) \propto \exp(-ES)$ with I the emitted electron current at energy E and S the slope of $2.3 \pm 0.2\ eV^{-1}$ comparable with other values reported before [S16]. An effective temperature $T_{eff} = 1/Sk_B$ (k_B is the Boltzmann constant) of 5100 ± 525 K can be extracted from the inverse of the slope of these data (see figure S18). This effective temperature is rather constant while the laser power has been changed by more than an order of magnitude. As this temperature is above the melting temperature of tungsten and is independent of the laser power, this slope is not related to the average thermodynamic temperature of the tip. It may be considered as a crude estimate of a time averaged temperature of the emitted electrons during the pulse, although the definition of such a temperature is questionable in this out of equilibrium regime where the electron distribution can present multi-photonic

steps and did not relax to a Fermi-Dirac distribution. This behavior of the high energy emitted electrons is rather similar to what was previously observed on clean metallic tips and our simulations shown below confirms that the presence of a nano-object is not expected to influence this part of the electron energy spectrum. The presence of a faint peak above E2 in the simulations at the highest power in Fig. 3 b of the main text, is due to the multiphotonic electronic distribution that did not relax yet to a thermalized Fermi-Dirac distribution (the faint peak corresponds to $3h\nu$). This faint peak is not visible in the experimental curves probably because the simulations do not take into account: i) the shot noise that makes this peak more difficult to detect, ii) additional scattering mechanisms at the interface between the tip and the quantum dot that may relax faster the electronic distribution.

D. Effective cross section of QD1:

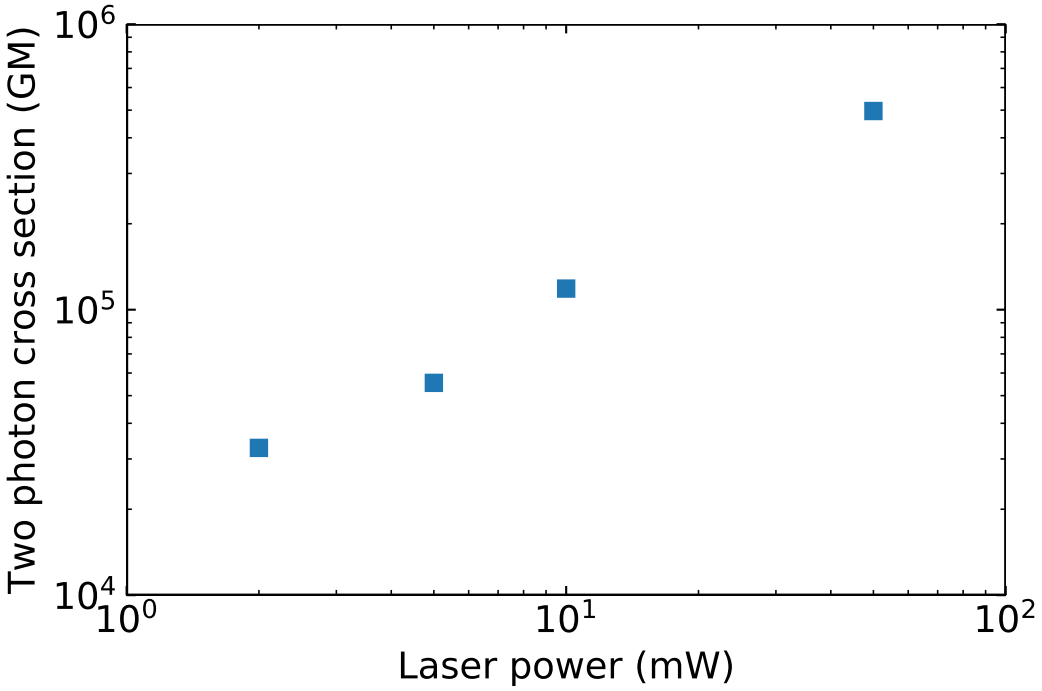

FIG. S19: Two photon cross section of QD1 as a function of the laser intensity for an applied voltage of $V_{DC} = 290$ V.

From the energy distribution of the emitted electron shown in Fig. 3 of the main text, the integrated intensity of the high energy peak centered at an energy E_2 is calculated. This

value is then used in the theoretical formula of the 2 photon cross section [S17] given in the main text in order to plot the effective cross section in units of GM (Goeppert Mayer) as a function of the laser power in Fig. S19. This cross section is too high for a quantum dot as discussed in the main text.

IV. NUMERICAL SIMULATIONS OF THE ELECTRON EMISSION UNDER LASER ILLUMINATION

The electron energy distributions of a quantum dot illuminated by a femtosecond laser is calculated by solving the 1D Schrödinger equation without the laser and calculating from the Boltzmann equation, the out of equilibrium electron energy distribution generated by the laser.

A. Expression of the field emission current:

Usually theoretical studies of field emission assume that the electrons come from a 3D material and have to tunnel through a 1D barrier in the direction parallel to the principal tip axis (noted as //). In this approach, the hamiltonians in the parallel // and perpendicular (noted as $\perp$) directions commute. Thus the calculation can be treated in 1D taking into account only tunneling in the parallel direction.

The total current density flowing in the // direction is :

$$J_{tot} = 2 \int \int \int n(\vec{k}) e v_{//} T(k_{//}, F) f(k) dk_{//} k_{\perp} dk_{\perp} d\varphi \tag{S4}$$

where the factor 2 is for the spin, e is the electron charge, n the number of charge carrier per volume unit and J_{tot} in A/cm^2, $v_{//}$ is the electron speed in the // direction, T is 1D the transmission of the barrier, f(k) is the electron distribution given by the Fermi Dirac distribution at equilibrium, $k_{//}$ is the electron wave vector in the // direction, $k_{\perp}$ is the electron wave vector amplitude in the $\perp$ direction and φ is the angle of the $k_{\perp}$ vector in the $\perp$ plane,

$$\rho(\vec{k}) \vec{dk}^3 = \left(\frac{L}{2\pi} \right)^3 \vec{dk}^3 \tag{S5}$$

and so the density is:

$$n(\vec{k}) = \frac{\rho(\vec{k})}{L^3} \tag{S6}$$

In our experiments, the transmission and the electron energy distributions are drastically different than in the classical field emission case. The calculations of these quantities are given in the next paragraphs.

B. Analytical calculation of the transmission of the quantum dot:

A first step in calculating the transmission of a quantum dot on a field emission tip is to assume a Lorentzian shape [S18] of the resonant energy level. However this resonant tunneling model gives rather crude and inaccurate electron energy distributions. Instead, here we solve analytically the 1D Schrödinger equation in the absence of image charge.

The expression of the potential in and out the metallic tip is given by :

$$V(x) = 0, x < 0 \tag{S7}$$

$$V(x) = \phi + E_F - eFx, x \in [0; d] \tag{S8}$$

$$V(x) = \phi + E_F - eFx - V_0, x \in [d; d + a] \tag{S9}$$

$$V(x) = \phi + E_F - eFx, x > d + a \tag{S10}$$

where d is the width of the first barrier and a the size of the quantum dot (QD), x is the position in the // direction and $x = 0$ the position of the interface between the tip and vacuum, ϕ the work function, E_F the Fermi energy, F the electric field, $e > 0$ the charge of the electron and V_0 the potential in the quantum dot at zero field. As explained in section I G and in ref. [S10], the barrier of width d may be a contamination layer or an interface between tungsten and carbon mono-oxide and thus should have a thickness smaller than 1 nm. The potential barrier is shown in Fig. S20.

In the calculations, the reference of the energy is taken from the bottom of the conduction band but in the illustrations the energy is referenced from the Fermi energy in the metal for convenience.

For $x < 0$ the solution of the Schrödinger equation is :

$$\psi_I(x) = Ae^{ikx} + Be^{-ikx} \tag{S11}$$

with A and B two complex constants, $k = \sqrt{2mE_{//}}/\hbar$, m the electron mass and $E_{//}$ the electron energy in the direction of electron propagation. As in the usual Fowler Nordheim model [S19], we consider that the system is invariant in the transverse direction.

For $x \in [0, d]$, we have :

$$\psi_{II}(x) = CA_i(\alpha^*(x - L)) + DB_i(\alpha^*(x - L))] \tag{S12}$$

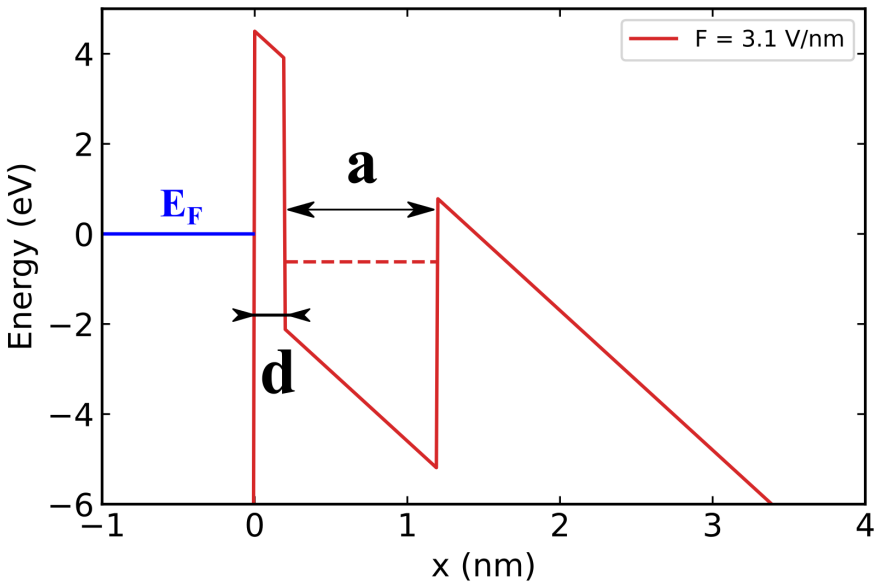

FIG. S20: Simplified 1D potential barrier for a quantum dot at the apex of a metallic field emitter. The horizontal line for $x < 0$ represents the position of the Fermi Energy inside the metal. The dotted line represent the position of a resonant energy level inside the quantum dot according to analytical calculations for F = 3.1 V/nm, d = 0.2 nm and a = 1 nm.

where we defined $\alpha = (2meF/\hbar^2)^{1/3} = -\alpha^*$ and the tunneling length L given by :

$$V(L) = \phi + E_F - eFL = E_{//} \tag{S13}$$

So :

$$L = \frac{\phi + E_F - E_{//}}{eF} \tag{S14}$$

A_i and B_i are the Airy functions.

For $x \in [d, d+a]$ inside the QD, we have :

$$\psi_{III}(x) = E_0[iA_i(\alpha^*(x-L_0))+B_i(\alpha^*(x-L_0))]+F_0[-iA_i(\alpha^*(x-L_0))+B_i(\alpha^*(x-L_0))] \tag{S15}$$

with

$$L_0 = \frac{\phi + E_F - V_0 - E_{//}}{qF} \tag{S16}$$

For $x > d + a$, we have :

$$\psi_{IV}(x) = G[iA_i(\alpha^*(x-L)) + B_i(\alpha^*(x-L))] \tag{S17}$$

Then for x = 0 we equal the wave functions and its derivatives on each side of the interface :

$$\begin{aligned} A + B &= CA_i(\alpha L) + DB_i(\alpha L) \\ ikA - ikB &= -\alpha CA_i'(\alpha L) - \alpha DB_i'(\alpha L) \end{aligned} \tag{S18}$$

With matrix notation this gives :

$$M_{0n}= \begin{pmatrix} 1 & 1 \\ ik & -ik \end{pmatrix}, M_{0p}= \begin{pmatrix} A_i(\alpha L) & B_i(\alpha L) \\ -\alpha A_i'(\alpha L) & -\alpha B_i'(\alpha L) \end{pmatrix}$$

$$M_{0n} \begin{pmatrix} A \\ B \end{pmatrix} = M_{0p} \begin{pmatrix} C \\ D \end{pmatrix}$$

For x = d,with matrix notation we have :

$$M_{dn}= \begin{pmatrix} A_i(\alpha(L-d) & B_i(\alpha(L-d) \\ A_i'(\alpha(L-d)) & B_i'(\alpha(L-d)) \end{pmatrix}$$

$$M_{dp}= \begin{pmatrix} B_i(\alpha(L_0-d)) + iA_i(\alpha(L_0-d) & B_i(\alpha(L_0-d)) - iA_i(\alpha(L_0-d) \\ B_i'(\alpha(L_0-d)) + iA_i'(\alpha(L_0-d) & B_i'(\alpha(L_0-d)) - iA_i'(\alpha(L_0-d) \end{pmatrix}$$

$$M_{dn} \begin{pmatrix} C \\ D \end{pmatrix} = M_{dp} \begin{pmatrix} E_0 \\ F_0 \end{pmatrix}$$

For x = d+a,we have :

$$M_{dan}= \begin{pmatrix} B_i(\alpha(L_0-d-a)) + iA_i(\alpha(L_0-d-a) & B_i(\alpha(L_0-d-a)) - iA_i(\alpha(L_0-d-a) \\ B_i'(\alpha(L_0-d-a)) + iA_i'(\alpha(L_0-d-a) & B_i'(\alpha(L_0-d-a)) - iA_i'(\alpha(L_0-d-a) \end{pmatrix}$$

$$M_{dap}= \begin{pmatrix} B_i(\alpha(L-d-a)) + iA_i(\alpha(L-d-a) & 0 \\ B_i'(\alpha(L-d-a)) + iA_i'(\alpha(L-d-a) & 0 \end{pmatrix}$$

$$M_{dan}\begin{pmatrix}E_0\\F_0\end{pmatrix}=M_{dap}\begin{pmatrix}G\\0\end{pmatrix}$$

So :

$$\begin{pmatrix}A\\B\end{pmatrix}=M_{0n}^{-1}M_{0p}M_{dn}^{-1}M_{dp}M_{dan}^{-1}M_{dap}\begin{pmatrix}G\\0\end{pmatrix}$$

We deduce the transmission from :

$$T=\frac{|A|^2-|B|^2}{|A|^2} \tag{S19}$$

We can set G = 1 and get A and B from the matrix product, however to get a more accurate value of $|A|^2-|B|^2$ for low transmission it is better to develop the calculation and make some simplification :

$$A^2-B^2=16\alpha k\Delta^2 W_{Ai}(\alpha L)W_{Ai}(\alpha(L-d))W_{Ai}(\alpha(L_0-d))W_{Ai}(\alpha(L_0-d-a))W_{Ai}(\alpha(L-d-a)) \tag{S20}$$

with W_{Ai} the Wronskian of Airy functions whose value is independent of z :

$$W_{Ai}(z)=A_i(z)B_i'(z)-A_i'(z)B_i(z)=\frac{1}{\pi} \tag{S21}$$

and

$$\Delta=det(M_{0n})det(M_{dn})det(M_{dan}) \tag{S22}$$

We performed numerical simulations for 2 different quantum dots in order to reproduce the experimental data of Fig. 1b of the main text (corresponding to the sample called QD11) and Fig. 2 and 3 (corresponding to the sample called QD1). As explained in the main text a, d and V_0 have been selected in order to reproduce the spacing and voltage dependence of the energy levels in the experiment. "a" has a strong influence on the voltage dependence of the energy levels and the energy spacing between levels. "V_0" plays an important role to determine the position of the energy levels. "d" modifies the voltage dependence of the energy levels and the width of the peaks. The value of the parameters used in the simulations are : $\phi = 4.5$ eV, $E_F = 9.2$ eV, d = 0.1 nm, a = 1.4 nm, $V_0 = 6.2$ eV for QD1 and d = 0.2 nm, a = 1.0 nm, $V_0 = 6$ eV for QD11. An example of the calculated transmission of QD1 is given in Fig. S21.

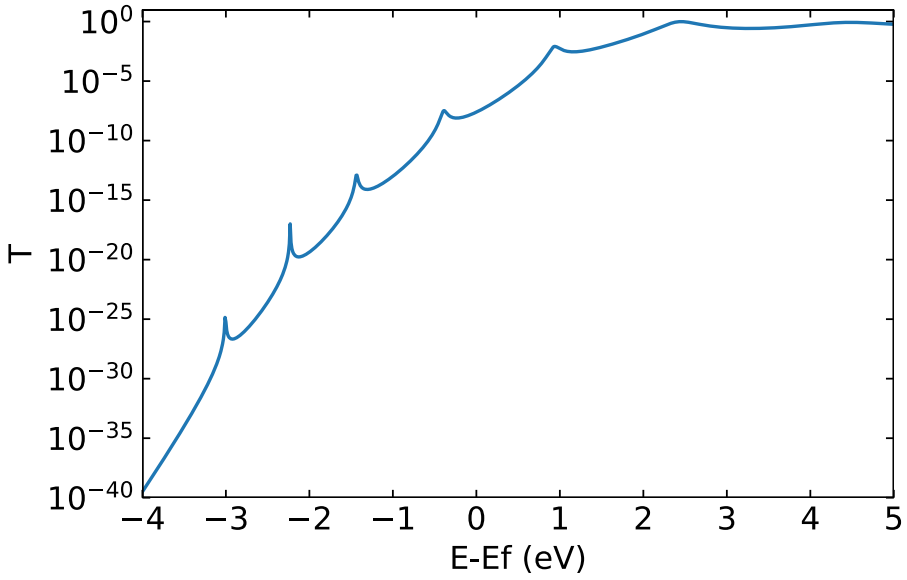

FIG. S21: Calculated transmission for QD1 for F = 1.47 V/nm, i.e same parameters as used for Fig. 3b in the main text. The peaks in the transmission correspond to the different resonant electron energy levels.

C. Numerical calculation of the out of equilibrium electron distribution:

The femtosecond laser pulse is modelized by a Gaussian function :

$$P(t) = A_e \exp(-t^2/\sigma^2) \tag{S23}$$

with A_e a constant proportional to the laser intensity, t the time and $\sigma = \tau/\sqrt{4ln(2)}$ where $\tau = 14$ fs is the pulse duration given in the main text (full width at half maximum : FWHM).

The electron distribution f(k,t) is considered as in equilibrium at room temperature 70 fs before the arrival of the laser pulse (the starting time has been chosen 10 times larger than the half width of the pulse) and equal to the Fermi Dirac distribution. The evolution of f(k,t) is calculated by solving the electron Boltzmann equation [S2, S20, S21] for each time every $\Delta t = 0.1$ fs :

$$f(k, t + \Delta t) = f(k, t) + \left.\frac{\partial f}{\partial t}\right|_{abs} \Delta t + \left.\frac{\partial f}{\partial t}\right|_{el-el} \Delta t + \left.\frac{\partial f}{\partial t}\right|_{el-p} \Delta t \tag{S24}$$

where we have included the absorption of photon energy $h\nu$:

$$\left.\frac{\partial f}{\partial t}\right|_{abs} = P(t)\left(\sqrt{E-h\nu}f(E-h\nu)[1-f(E)] - \sqrt{E+h\nu}f(E)[1-f(E+h\nu)]\right) \quad \text{(S25)}$$

with $E = \hbar^2k^2/2m$ the electron energy; the electron-electron scattering :

$$\left.\frac{\partial f}{\partial t}\right|_{el-el} = \frac{me^4}{32\pi^3\hbar^3\epsilon_0^2 E_S\sqrt{E_S}}\int dE_1 dE_2 [\frac{\sqrt{\tilde{E}}}{\tilde{E}+E_S} + \frac{1}{\sqrt{E_S}}]_{\tilde{E}_{min}}^{\tilde{E}_{max}} F(E,E_1,E_2,E_3) \quad \text{(S26)}$$

with E and E_1 the energies of the incident electrons, E_2 and E_3 the energies of the scattered electrons, $E_S = \frac{\hbar^2k_S^2}{2m}$ and $k_S^2 = \frac{e^2m_e}{\pi^2\hbar^2\epsilon_0}\int_0^{+\infty} f(k)dk$

$\tilde{E}_{min} = min[(\sqrt{E_1}+\sqrt{E_3})^2; (\sqrt{E}+\sqrt{E_2})^2]$

$\tilde{E}_{max} = max[(\sqrt{E_1}-\sqrt{E_3})^2; (\sqrt{E}-\sqrt{E_2})^2]$

$$F(E,E_1,E_2,E_3) = [1-f(E)][1-f(E_1)]f(E_2)f(E_3) - f(E)f(E_1)[1-f(E_2)][1-f(E_3)] \quad \text{(S27)}$$

and the electron-phonon scattering:

$$\left.\frac{\partial f}{\partial t}\right|_{el-p} = \frac{me^2}{4\pi\epsilon_0\hbar^3}\frac{1}{k}\int_0^{q^*} dq\frac{q^2E_p(q)}{q^2+k_S^2}\Sigma_{+/-}S^{+/-}(k,q,t) \quad \text{(S28)}$$

where $q^* = min(q_D, \frac{m}{\hbar}v_S + k)$, q_D is the Debye wave number, corresponding to a Debye temperature of 400K.

$S^+(k,t) = f(k+q,t)(1-f(k,t))(1+g(q,t)) - f(k,t)(1-f(k+q,t))g(q,t)$

$S^-(k,t) = f(k-q,t)(1-f(k,t))(1+g(q,t)) - f(k,t)(1-f(k+q,t))g(q,t)$

$E_p(q) = \hbar v_{sd}q$ is the phonon energy, $v_{sd} = 5220$ m/s is the sound velocity, g(q,t) is the phonon distribution with a wave vector q and its evolution is described by a Boltzmann equation with

$g(q,t+\Delta t) = g(q,t) + \left.\frac{\partial g}{\partial t}\right|_{el-p}\Delta t$

where the initial phonon distribution is the Bose Einstein distribution and this distribution is excited by the electron-phonon coupling given by :

$$\left.\frac{\partial g}{\partial t}\right|_{el-p} = \frac{me^2}{2\pi\epsilon_0\hbar^3}\frac{1}{q}\frac{E_p(q)}{q^2+k_S^2}\int_0^{k^*} kdkS^+(k,q) \quad \text{(S29)}$$

Fig. S22 shows an example of the temporal evolution of the distribution of electrons for two laser powers. The electron pulse at 10 mW has a FWHM of 12.9 fs slightly smaller than

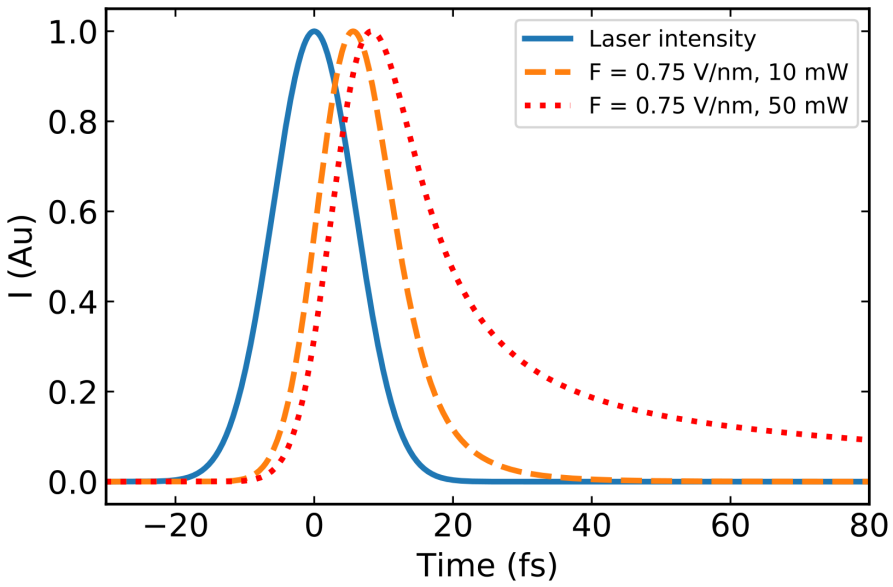

FIG. S22: Calculated laser and electron pulses for 10 and 50 mW at an electron energy of E_2 = 3.08 eV corresponding to the maximum of the transmission of QD1. The amplitude of the pulses have been renormalized for clarity.

the original laser pulse of 14 fs and a delay of 5.6 fs. This modification of the pulse duration is due to the relaxation dynamics of the electrons and is dominated at this time scale by the electron-electron interaction. In the range of energy for E_2 explored in our experiments (between 2.5 and 3 eV) the FWHM and delay doesn't change significantly (less than 1 fs). To the contrary, for 50 mW, the temporal response of the electron tends to worsen, the FWHM increases up to 17.4 fs and the time delay is of 8.3 fs.

Compared to DC field emission, femtosecond laser excitation permits to create an ultrafast non-stationary electron distribution. The energy gained by the electrons from the photons allows the electrons to tunnel from the tip to the quantum dot higher energy levels. These states can therefore be observed in laser induced resonant tunneling. Because the laser pulse is short, the multiphoton absorption has to occur within a few fs and the non-stationary electron distribution is created at this timescale where electron-phonon and even electron-electron scattering is rather limited

D. Expression of the electron energy distribution:

A retarding field energy analyzer performs a spectroscopy of the electron energy distribution by repelling the electrons with a kinetic energy lower than the sum of the grid work function and the grid voltage. As this repelling electrostatic force is mostly perpendicular to the grid surface, it filters the normal (or radial in a spherical geometry) electron energy. However it has been noticed that the measured energy spectrum corresponds to the total energy and not the normal energy [S13]. This discrepancy can be simply explained by the tip geometry and the conservation of the electron angular momentum. The electrostatic force bends the electron trajectories and rapidly converts the transverse energy to the normal energy as explained in the review paper of Gadzuk [S18]. The expression of the total energy distribution [S12] is then obtained by integrating only along the transverse energy term inside the integral of equation S4 to give:

$$J_{TED}(E) = \frac{1}{2\pi^2}\frac{me}{\hbar^3}\frac{1}{1+\exp\left(\frac{E-E_F}{k_BT}\right)}\left(\int_{E_{//}=0}^{E} T(E_{//},F)dE_{//}\right) \tag{S30}$$

However for a quantum dot this demonstration doesn't hold as the emitter shape differs significantly from the simple spherical geometry. We found that a description in terms of the normal energy distribution was closer to the measured electron energy spectrum. So we used the expression of the normal energy distribution [S12] obtained from equation S4 and an integration on the energy E while keeping the energy $E_{//}$ constant:

$$J_{NED} = \frac{1}{2\pi^2}\frac{mek_BT}{\hbar^3}T(E_{//},F)\ln\left[1+\exp\left(\frac{E_F-E_{//}}{k_BT}\right)\right] \tag{S31}$$

Moreover, this expression is only valid in the equilibrium case as it uses the expression of the Fermi Dirac distribution. So, under laser illumination,the integration on the energy E has to be done numerically with the non-equilibrium distributions calculated previously. Finally, this theoretical expression has to be convoluted with the resolution of our energy analyzer. It is assumed that our analyzer has a Gaussian transmission function with a standard deviation of 250 meV ($\sim$ 0.41 eV of FWHM).

[S1] R. H. Good and E. W. Müller, in *Electron-Emission Gas Discharges I/Elektronen-Emission Gasentladungen I* (Springer, 1956), pp. 176–231.

[S2] H. Yanagisawa, M. Hengsberger, D. Leuenberger, M. Klöckner, C. Hafner, T. Greber, and J. Osterwalder, Physical review letters **107**, 087601 (2011).

[S3] M. Krüger, M. Schenk, and P. Hommelhoff, Nature **475**, 78 (2011).

[S4] G. Herink, D. Solli, M. Gulde, and C. Ropers, Nature **483**, 190 (2012).

[S5] P. C. Bettler and F. M. Charbonnier, Phys. Rev. **119**, 85 (1960).

[S6] V. T. Binh, S. Purcell, N. Garcia, and J. Doglioni, Physical review letters **69**, 2527 (1992).

[S7] S. Purcell, V. T. Binh, and N. Garcia, Applied physics letters **67**, 436 (1995).

[S8] L. Y. Ming, N. D. Lang, B. W. Hussey, T. P. Chang, and W. A. Mackie, Physical review letters **77**, 1636 (1996).

[S9] X. Zhao, R. Outlaw, R. Champion, J. Wang, D. Manos, and B. Holloway, Applied physics letters **85**, 1415 (2004).

[S10] K. Nagaoka, H. Fujii, K. Matsuda, M. Komaki, Y. Murata, C. Oshima, and T. Sakurai, Applied surface science **182**, 12 (2001).

[S11] N. Saitou and S. Yamamoto, Applications of Surface Science **5**, 374 (1980).

[S12] R. D. Young, Physical Review **113**, 110 (1959).

[S13] R. D. Young and E. W. Müller, Physical Review **113**, 115 (1959).

[S14] A. J. Bennett and L. Falicov, Physical Review **151**, 512 (1966).

[S15] M. Lin, R. Andres, and R. Reifenberger, Physical review letters **67**, 477 (1991).

[S16] S. V. Yalunin, G. Herink, D. R. Solli, M. Krüger, P. Hommelhoff, M. Diehn, A. Munk, and C. Ropers, Annalen der Physik **525**, L12 (2013).

[S17] S. A. Blanton, A. Dehestani, P. C. Lin, and P. Guyot-Sionnest, Chemical physics letters **229**, 317 (1994).

[S18] J. W. Gadzuk and E. Plummer, Reviews of Modern Physics **45**, 487 (1973).

[S19] R. H. Fowler and L. Nordheim, Proceedings of the Royal Society of London. Series A **119**, 173 (1928).

[S20] N. Del Fatti, C. Voisin, M. Achermann, S. Tzortzakis, D. Christofilos, and F. Vallée, Phys. Rev. B **61**, 16956 (2000), URL `https://link.aps.org/doi/10.1103/PhysRevB.61.16956`.

[S21] C. Voisin, *Étude femtoseconde de la dynamique électronique et vibrationnelle dans des nanoparticules métalliques* (PhD thesis Université Paris Sud - Paris XI, 2001), URL `https://tel.archives-ouvertes.fr/tel-00175114v1`.